Front. Med. 2024, 18(1): 81−97
https://doi.org/10.1007/s11684-023-1006-x

RESEARCH ARTICLE

Panoramic variation analysis of a family with neurodevelopmental disorders caused by biallelic loss-of-function variants in *TMEM141*, *DDHD2*, and *LHFPL5*

Liwei Sun[1,2,3,*], Xueting Yang[1,*], Amjad Khan (✉)[1,4,5,6,*], Xue Yu[1,7], Han Zhang[1,8], Shirui Han[1], Xiaerbati Habulieti[1], Yang Sun[1], Rongrong Wang (✉)[1], Xue Zhang[1]

[1]*McKusick-Zhang Center for Genetic Medicine, State Key Laboratory for Complex Severe and Rare Diseases, Institute of Basic Medical Sciences Chinese Academy of Medical Sciences, School of Basic Medicine Peking Union Medical College, Beijing 100005, China;* [2]*Chongqing Key Laboratory of Human Embryo Engineering, Center for Reproductive Medicine, National Key Clinical Speciality Construction Project (Obstetrics and Gynecology), Chongqing Health Center for Women and Children, Chongqing 400013, China;* [3]*Chongqing Clinical Research Center for Reproductive Medicine, Women and Children's Hospital of Chongqing Medical University, Chongqing 400013, China;* [4]*Faculty of Biological Sciences, Department of Zoology, University of Lakki Marwat, Khyber Pakhtunkhwa 28420, Pakistan;* [5]*Institute for Medical Genetics and Applied Genomics, University of Tübingen, Tübingen 72076, Germany;* [6]*Alexander von Humboldt fellowship Foundation, Berlin 10117, Germany;* [7]*Department of Pediatrics, the First Affiliated Hospital of Guangxi Medical University, Nanning 530000, China;* [8]*Department of Laboratory Medicine, State Key Laboratory for Complex Severe and Rare Diseases, Peking Union Medical College Hospital, Chinese Academy of Medical Science and Peking Union Medical College, Beijing 100730, China*

Abstract **Highly clinical and genetic heterogeneity of neurodevelopmental disorders presents a major challenge in clinical genetics and medicine. Panoramic variation analysis is imperative to analyze the disease phenotypes resulting from multilocus genomic variation. Here, a Pakistani family with parental consanguinity was presented, characterized with severe intellectual disability (ID), spastic paraplegia, and deafness. Homozygosity mapping, integrated single nucleotide polymorphism (SNP) array, whole-exome sequencing, and whole-genome sequencing were performed, and homozygous variants in *TMEM141* (c.270G>A, p.Trp90*), *DDHD2* (c.411+767_c.1249-327del), and *LHFPL5* (c.250delC, p.Leu84*) were identified. A *Tmem141*$^{p.Trp90*/p.Trp90*}$ mouse model was generated. Behavioral studies showed impairments in learning ability and motor coordination. Brain slice electrophysiology and Golgi staining demonstrated deficient synaptic plasticity in hippocampal neurons and abnormal dendritic branching in cerebellar Purkinje cells. Transmission electron microscopy showed abnormal mitochondrial morphology. Furthermore, studies on a human *in vitro* neuronal model (SH-SY5Y cells) with stable shRNA-mediated knockdown of *TMEM141* showed deleterious effect on bioenergetic function, possibly explaining the pathogenesis of replicated phenotypes in the cross-species mouse model. Conclusively, panoramic variation analysis revealed that multilocus genomic variations of *TMEM141*, *DDHD2*, and *LHFPL5* together caused variable phenotypes in patient. Notably, the biallelic loss-of-function variants of *TMEM141* were responsible for syndromic ID.**

Keywords neurodevelopmental disorder; autosomal recessive intellectual disability; consanguinity; spastic paraplegia; hearing loss; *TMEM141*

Introduction

Neurodevelopmental disorders (NDDs) belong to a class of disorders affecting brain development and function, including intellectual disability (ID), autism spectrum disorder, and attention deficit hyperactivity disorder [1].

Received December 8, 2022; accepted April 27, 2023

Correspondence: Rongrong Wang, rongrongbwl@ibms.pumc.edu.cn;
Amjad Khan, amjadkhanqau123@hotmail.com

*These authors contributed equally to the study.

ID is characterized by substantial limitations in intellectual functioning and adaptive behavior [2] and is a genetically and clinically heterogeneous disorder that can be accompanied by impairments in motor skills, speech, and social activities. It has a prevalence of approximately 1% worldwide, presenting a major challenge in clinical genetics and medicine [3]. However, the genetic diagnosis of ID remains lacking in most cases [4]. Autosomal recessive (AR) gene defects are the leading genetic causes of ID in countries with frequent parental consanguinity, accounting for approximately 1/7th of the world's population [5]. Next-generation sequencing (NGS) reveals novel genetic variants that will expand our understanding of disease causality and facilitate accurate diagnosis. Notably, NGS can provide insights into the relationship between multilocus genomic variation and disease, particularly when genetically and clinically heterogeneous diseases, such as NDDs, are considered.

Many transmembrane (TMEM) proteins localized mainly to mitochondria, endoplasmic reticulum, lysosomes, and Golgi apparatus cause severe neurological disorders. For example, variants in *TMEM65* (MIM *616609), *TMEM70* (MIM *612418), *TMEM147* (MIM *613585), *TMEM63C* (MIM *619953), and *TMEM67* (MIM *609884) can cause overlapping or somewhat distinct neurological manifestations [6–10]. Transmembrane protein 141 (*TMEM141*) has a genomic size of 1974 bp with five coding exons. A full-length *TMEM141* messenger RNA (mRNA) encodes a 108-amino-acid transmembrane protein mainly localized in mitochondria. A missense variant (c.162 G>C; p.Arg54Ser) in *TMEM141* was found in a Utah pedigree with a high risk for suicide [11], indicating its potential role in neuronal function and psychiatric conditions. However, little is known about the function of *TMEM141*; therefore, its specific function remains to be extensively investigated.

Here, we describe a patient from a consanguineous family presenting with severe ID, spastic paraplegia, and deafness, which were apparent from early childhood. Through pedigree analysis, single nucleotide polymorphism (SNP) array analysis, whole-exome sequencing (WES), whole-genome sequencing (WGS), and functional studies, we performed panoramic variation analysis of this NDD family [12] and identified the recurrent c.250delC (p.Leu84*) variant in *LHFPL5* (NM_182548.4), which causes deafness; a novel intragenic deletion, c.411+767_c.1249-327del, in *DDHD2* (NM_001164232.2), which causes spastic paraplegia; and a novel homozygous nonsense variant, c.270 G>A (p.Trp90*), in *TMEM141* (NM_032928.4), which might explain the ID and movement impairment phenotypes of the patient. To elucidate the function of *TMEM141*, we generated and analyzed mice homozygous for the human variant in the mouse *tmem141* ortholog. Then, we performed panoramic variation analysis of an NDD patient with parental consanguinity and identified biallelic loss-of-function (LoF) variants in three different genes: *LHFPL5* (MIM *609427), *DDHD2* (MIM *615003), and the functionally characterized *TMEM141*, accounting for her complex NDD phenotypes.

Materials and methods

Ethical approval and family history

One Pakistani family with severe ID, spastic paraplegia, and deafness was recruited for the present study. Clinical information, family history, and peripheral blood samples were collected from the affected individual and unaffected individuals in the family after written informed consent was obtained from each family member. The study design was approved by the institutional review board of Chinese Academy of Medical Science and Peking Union Medical College and was performed in accordance with the *Helsinki Declaration*. Animal care and experiments were approved by the institutional animal care and use committee of the Chinese Academy of Medical Science and Peking Union Medical College.

DNA extraction, SNP 6.0 arrays, WES, and WGS

Genomic DNA was extracted from peripheral blood samples using a QIAamp DNA blood midi kit (Qiagen, Hilden, Germany) and quantified using a Nanodrop 2000 spectrophotometer (Thermo Scientific, MA, USA). First, Affymetrix SNP6.0 arrays were used in assessing copy number variants (CNVs). Homozygosity mapping was performed for the mapping of recessive traits in the consanguineous family. WGS and WES were performed on the proband and parents for the identification of the underlying genetic variants in the family. Briefly, an NEB Next Ultra DNA library prep kit for Illumina (NEB, MA, USA) was applied for library preparation in WGS, and an Agilent liquid capture system (Agilent SureSelect Human All Exon V6, Agilent Technologies, CA, USA) was used to enrich exome sequences for library preparation in WES. Finally, DNA libraries were sequenced on an Illumina platform, and 150 bp paired-end reads were generated. After data quality control, the obtained reads were mapped to the GRCh37/hg19 reference genome database with Burrows Wheeler Aligner (BWA, 0.7.8-r455) software. For variant detection, SAMtools (v.1.6), CoNIFER (v.0.2.2), and Lumpy were used to identify SNPs, InDels, CNVs, and SVs, and then the data were annotated by ANNOVAR (v.2017Jun01) for subsequent analysis. Integrative Genome Viewer (IGV) was used for sequence data visualization. The functional consequences of variants were assessed using different *in silico* algorithms in the VarCards database. Effects on splicing

were evaluated using Human Splicing Finder [13]. Candidate variants were assessed using the following criteria: (1) frequency of less than 1% in public databases, including the 1000 Genomes database and Genome Aggregation Database (gnomAD); (2) location within a coding sequence or near splicing sites; (3) nonsynonymous variants; (4) location within the homozygosity mapping region; (5) not compound heterozygous and *de novo* variants. Sanger sequencing was performed to validate the identified variants in all available family members. The *TMEM141* nonsense variant was genotyped in DNA samples from 200 unrelated control subjects.

RNA extraction, cDNA synthesis, and quantitative RT–PCR (qRT–PCR)

Total RNA was isolated from peripheral blood leukocytes by using TRIzol LS (Invitrogen, CA, USA), and 2 μg of RNA was subjected to reverse transcription with PrimeScript RT Master Mix (Takara Bio, Dalian, China) according to the manufacturer's protocol. qRT-PCR was performed using SYBR Premix Ex Taq (Takara Bio, Dalian, China) on a Rotor-Gene 6000 (Qiagen, Hilden, Germany) instrument. The amplification conditions were as follows: 10 min at 95 °C and 40 cycles of 10 s at 95 °C, 15 s at 60 °C, and 20 s at 72 °C. All the reactions were run in triplicate, and glyceraldehyde 3-phosphate dehydrogenase (GAPDH) was used as an endogenous control. The relative amounts of *TMEM141* mRNA were calculated using the $2^{-\Delta\Delta Ct}$ method and Roter-Gene Q series software (Qiagen, Hilden, Germany).

Vector construction and HEK293T cell culture

To observe mutant TMEM141 protein expression and localization *in vitro*, wild-type (WT) human *TMEM141* and mutant *TMEM141* (p.Trp90*) were constructed and then recombined with the eukaryotic expression vector pcDNA3.1. FLAG-tag was fused at the N-terminus of WT and mutant *TMEM141*. Human HEK293T cells, obtained from American Tissue Culture and Collection, were cultured in Dulbecco's modified Eagle's medium (Gibco, MA, USA) supplemented with 10% fetal bovine serum (FBS; Life Technologies, USA), penicillin (100 U/mL), and streptomycin (100 U/mL) at 37 °C in 5% CO_2. When the cells reached 60%–70% confluence, the same amounts of plasmids were transfected using Lipofectamine 3000 (Thermo Fisher Scientific, MA, USA) according to the manufacturer's instructions.

Human SH-SY5Y neuroblastoma cell culture and lentiviral infection of SH-SY5Y cells

SH-SY5Y cells were grown on cover slips at 37 °C and 5% CO_2 in an RPMI 1640 medium supplemented with 15% FBS and 100 U/mL penicillin/streptomycin. To silence *TMEM141*, pHBLV-U6-MCS-CMV-ZsGreen-PGK-PURO lentiviral vectors with puromycin-resistant genes were used (Hanbio Biotechnology, Shanghai, China). The following three shRNAs with different target sequences were used: GAGGAAGTTTCCATACCCTTT (*TMEM141*-RNAi-1), CAAAGACAGGAGCACAGATCA (*TMEM141*-RNAi-2), and GTCGGAGAAATGCAACAA CCT (*TMEM141*-RNAi-3). SH-SY5Y cells were plated into 12-well culture plates (5000/well) and infected with a lentivirus (MOI = 20) 24 h after the cells reached 70% confluence. Stable single clones were selected after 7 days of puromycin treatment (0.5 μg/mL). *TMEM141* expression in the stably infected clones was assessed using qRT-PCR and Western blot analysis. The shRNA with the highest silencing efficiency was selected.

Western blotting

A protease inhibitor and a phosphatase inhibitor (Roche, Basel, Switzerland) were added to the RIPA lysis buffer (Beyotime, Nantong, China) before the brain tissues or cultured cells were homogenized. The protein concentrations were measured using a BCA protein assay kit (Solarbio, Beijing, China), and equal amounts of protein (40 μg) were separated by sodium dodecyl sulfate–polyacrylamide gel electrophoresis (Bio-Rad Laboratories, CA, USA) and then transferred onto polyvinylidene difluoride (PVDF) membranes (Millipore, MA, USA). The PVDF membranes were blocked with 5% skim milk at room temperature for 1 h to prevent nonspecific binding, and immunoblots were incubated overnight at 4 °C with an anti-TMEM141 polyclonal antibody (16092-1-AP; Proteintech, IL, USA). After primary antibody binding, horseradish peroxidase-conjugated secondary antibodies were incubated for 1 h at room temperature. Equal loading was confirmed by reprobing membranes with antibodies against β-actin (BM0627; Boster, Wuhan, China) or GAPDH (5174; Cell Signaling Technology, MA, USA). Blots were developed using the ECL method, and band intensities were quantified using ImageJ Software.

Immunofluorescence staining

For cell culture, the cells plated on poly-D-lysine (Thermo Fisher Scientific, MA, USA)-coated coverslips were washed in PBS (20 mmol/L NaH_2PO_4 and 0.9% NaCl at pH 7.4) and fixed in 4% paraformaldehyde (PFA) for 20 min. The cells were then washed in PBS, permeabilized in PBS with 0.2% Triton X-100, incubated in blocking buffer (PBS with 1% BSA and 0.02% Triton X-100), and incubated with the following primary antibodies: anti-TMEM141 polyclonal antibody,

anti-NeuN (E4M5P) mouse mAb (94403; Cell Signaling Technology, MA, USA), and anti-Calbindin-D-28K monoclonal antibody (C9848; Sigma–Aldrich, MO, USA) in a blocking buffer at 4 °C overnight. The cells were subsequently washed in PBS and incubated for 1 h at room temperature with fluorescent secondary antibodies. After a series of washes, the coverslips were mounted on glass slides using antifade solution (AR1109; Boster, Wuhan, China). Confocal imaging was performed using an Olympus FV1000 confocal microscope.

For tissue sections, the mice were anesthetized and transcardially perfused with 4% PFA. The brains were dissected and postfixed at 4 °C in the same fixative. The tissues were then equilibrated in 15% and 30% sucrose until section preparation. Sagittal sections (10 μm) were cut using a Leica CM1950 microtome. For double immunofluorescence, free-floating sections were processed using Alexa Fluor 488-conjugated goat anti-rabbit/mouse or Alexa Fluor 594-conjugated goat anti-mouse/rabbit secondary antibodies.

Immunohistochemistry

After the mice were euthanized, cervical dislocation was performed. Mouse tissues were collected, fixed in 4% PFA, and embedded in paraffin. Immunohistochemistry was performed on 10 μm-thick sections of formalin-fixed and paraffin-embedded material. The deparaffinized sections were boiled in sodium citrate antigen retrieval solution (C1032; Solarbio, Beijing, China) for heat-induced epitope retrieval, rinsed in Tris-buffered saline (TBS) (pH 7.4), and kept in 0.3% H_2O_2 solution for 30 min to suppress endogenous peroxidase activity. The sections were then washed in TBS with 0.1% Tween (TBST) and blocked with 5% goat serum for 1 h at room temperature. The samples were incubated with anti-TMEM141 polyclonal antibody in an appropriate blocking buffer overnight at 4 °C. For light microscopy peroxidase staining, the sections were incubated with biotinylated secondary antibodies for 1 h at room temperature, washed in TBST, and incubated with avidin–biotinylated enzyme complex according to the manufacturer's instructions. Finally, the samples were washed with TBST and developed with 3,3′-diaminobenzidine (DAB), counterstained with hematoxylin and mounted using Permount mounting medium (KGF032; Keygen Biotech, Nanjing, China).

Electron microscopy of TMEM141 intramitochondrial localization

Enhanced ascorbate peroxidase (APEX), a 28 kDa genetically encodable electron microscopy tag, was used to localize the TMEM141 protein through intramitochondrial localization [14]. Briefly, we constructed a plasmid that would fuse *APEX*- to the C-terminus of *TMEM141*. Next, the plasmids were transfected into cultured HEK293T cells with Lipofectamine 3000 (Thermo Fisher Scientific, MA, USA). After 48 h, the transfected cells were fixed with 2.5% glutaraldehyde in 0.1 mol/L phosphate buffer (pH 7.4) for 1 h at room temperature and then were incubated in a freshly diluted solution of 0.5 mg/mL DAB tetrahydrochloride and 10 mmol/L hydrogen peroxide in 0.1 mol/L phosphate buffer (pH 7.4) for 30 min at 4 °C. Postfixation staining was performed using 1% osmium tetroxide for 1 h at 4 °C. The samples were rinsed for 10 min three times in chilled distilled water and then incubated in 2% aqueous uranyl acetate at 4 °C overnight. After gradient dehydration, the samples were infiltrated in epoxy resin and anhydrous ethanol with a volume ratio of 1:3 for 30 min, 1:1 overnight, and 3:1 overnight, and then infiltrated in 100% resin for 1 h three times and polymerized in a vacuum oven at 65 °C for 24 h. The sections were cut using an ultramicrotome (Leica EM FC7; Wetzlar, Germany) for 120 kV transmission electron microscopy (JEOL JEM-1400 Flash; Akishima-shi, Japan).

Generation of *Tmem141* $^{p.\ Trp90*/\ p.\ Trp90*}$ mice

Tmem141 knock-in (KI) mice were generated by CRISPR–Cas9, which was constructed by Nanjing Biomedical Research Institute of Nanjing University (Nanjing, China). The guide RNA (sequence: GTCAGAAATGCAGCAATCTC) was targeted to the mouse *Tmem141* exon 4, and a linearized donor vector was designed to introduce a nonsense variant into *Tmem141*. Cas9 mRNA, the donor vector, and single guide (sg) RNAs were coinjected into fertilized mouse eggs to generate targeted KI offspring. Transplantation into C57BL/6J mice was then performed. Pups were genotyped to obtain *Tmem141* KI mice. F0 founder animals were identified by PCR followed by sequence analysis and were bred to WT mice to test germline transmission and F1 animal generation.

M-mode echocardiography

To assess cardiac structure and function *in vivo*, noninvasive transthoracic echocardiography was performed using a Vevo 2100 high-resolution imaging system (40 MHz transducer; FUJIFILM VisualSonics, Toronto, Canada). The mice were anesthetized by inhalation of 2% isoflurane and placed in the supine position on the monitoring platform. The following parameters were measured: end-diastolic left ventricular anterior wall thickness (LVAW(d)), end-systolic left ventricular anterior wall thickness (LVAW(s)), end-diastolic left ventricular internal dimension (LVID(d)), end-systolic left ventricular internal dimension (LVID(s)),

end-diastolic left ventricular posterior wall thickness (LVPW(d)), and end-systolic left ventricular posterior wall thickness (LVPW(s)).

Magnetic resonance imaging (MRI)

Magnetic resonance imaging (MRI) was performed to evaluate brain structure in the mice. The mice were placed in a flow of warm air to maintain constant body temperature and were anesthetized by inhalation of 2% isoflurane. *In vivo* imaging of the mouse brain was performed using an Agilent 7T/R16 MRI scanner (Agilent Technologies, CA, USA).

Behavioral studies

We used 2-month-old WT and homozygous KI mice and sex- and age-matched controls in behavioral experiments according to a previous description with minor modifications [15,16]. Behavioral experiments were conducted during the light phase of the light/dark cycle between 9:00 a.m. and 5:00 p.m. Less stressful tests were performed first, and each behavioral test was separated by at least 4 days.

Morris water maze assay

Escape latency, swim distance, and swim speed were recorded using a camera and calculated using the SuperMaze system (Shanghai, China). First, the mice were trained to swim freely for 1 min. For the visible platform test, the mice were trained to locate an above-water platform with a visible cue for the first 2 days. For the hidden platform test, the mice were trained to find an unmarked and submerged platform for the next 4 days. The mice completed four trials from four different quadrants per training day. For the probe test on the final day, the platform was removed from the pool, and the mice swam for 1 min. The time spent in the quadrants and swimming speed were recorded.

Rotarod test

The mice were trained to run in a rotarod at a uniform acceleration speed of 4–40 rpm/min for 5 min. Speed and time to fall were recorded for each mouse to reflect motor performance. The mice completed three trials in a single day with an interval time of 30 min.

Step-down passive avoidance test

A step-down passive avoidance test was performed 1 day after the Morris water maze test as described in previous reports with minor modifications [17]. The equipment comprised five plastic black chambers with parallel stainless-steel grids, and a plastic platform was positioned in a corner of each chamber. Before the training session, the mice were gently placed on the grid floor, and each mouse was allowed to adapt for 5 min. Electric current (36 V) was delivered and maintained for 300 s. The mice would jump onto the platform to avoid the electric shock, and the number of errors of each mouse (number of times that the mouse stepped down from the platform) was recorded. After 24 h, retention test was performed, the electric shock was removed, the mice were placed on the platform, and the step-down latency of each mouse was recorded. The cutoff time in the training session and retention session were set at 300 s.

***In vitro* electrophysiology**

Slice preparation

Experiments were performed on 8-month-old C57/BL6 mice. Acute cerebellar slices were prepared from animals anesthetized with urethane (25%, 1 mL/100 g, Sigma–Aldrich, MO, USA). After decapitation, the brain was rapidly removed and transferred to ice-cold artificial cerebrospinal fluid for slicing (aCSF), where the hippocampus was isolated from the cortices. The aCSF contained 125 mmol/L NaCl, 2.5 mmol/L KCl, 1.25 mmol/L NaH_2PO_4, 25 mmol/L $NaHCO_3$, 10 mmol/L D-glucose, 2.0 mmol/L $CaCl_2$, and 1.5 mmol/L $MgCl_2$ (saturated with carbogen 95% O_2–5% CO_2). The isolated hippocampus was glued to an agar cube, and transverse slices with 380 μm thickness were cut using a slicer (Leica VT1200S, Wetzlar, Germany). The prepared hippocampal slices were recovered in oxygenated aCSF at 30 °C for at least 30 min and then incubated at room temperature for an additional 1 h before they were transferred to the recording chamber mounted on the stage of an upright microscope (Olympus BX50-WI, Tokyo, Japan), where they were continuously perfused with oxygenated aCSF by a peristaltic pump (BT100-2J; LongerPump, Baoding, China) at 7 mL/min and 30.5 ± 1 °C.

Electrophysiological recordings

Recordings were acquired using an Axopatch 700B amplifier and Digidata 1440A (Molecular Devices, CA, USA). Field excitatory postsynaptic potential (fEPSP) recordings were evoked by activating Shaffer collaterals with a stimulus pipette (1–2 MΩ) placed in the middle of the stratum radiatum in an area CA3 200–400 μm away from the recording pipette, which was placed in the middle of the stratum radiatum in area CA1, 75–150 μm deep into the tissue (Fig. 4A). The recording aCSF contained 125 mmol/L NaCl, 2.5 mmol/L KCl, 1.25 mmol/L NaH_2PO_4, 25 mmol/L $NaHCO_3$, 10 mmol/L

D-glucose, 2.0 mmol/L $CaCl_2$, and 1.0 mmol/L $MgCl_2$ (saturated with carbogen 95% O_2–5% CO_2). Square-wave current pulses (100 μs pulse width) were delivered using a stimulus isolator (Isoflex, AMPI, Jerusalem, Israel). For long-term recording, pulses at an intensity eliciting 40%–50% of the maximal response were delivered as the baseline level. After a stable baseline was recorded for at least 30 min, long-term potentiation (LTP) was induced by theta-burst stimulation (TBS). Two trains of 10 bursts (5 Hz) were delivered at 20 s intervals. Each burst comprised four pulses of 100 Hz. Following TBS, the stimulus frequency was returned to 30 s for 60 min. The early phase of LTP is the period 50–60 min after stimulation [18]. The slope of the fEPSP was measured by fitting a straight line of 20%–80% of the fiber volley to the fEPSP amplitude using Clamfit10.7 software. The mean value (%) of the last 10 min of the baseline was calculated to demonstrate the stability of the baseline and was compared with the mean value (%) of the sixth 10 min period after TBS induction. To compare the long-term synaptic plasticity between groups, significant differences were analyzed at the sixth 10 min period after TBS induction.

Golgi staining

Golgi-Cox impregnation was performed according to the manual of the Hito Golgi-Cox OptimStain kit (Hitobiotec, TN, USA). After the mice were deeply anesthetized, the brains of homozygous KI and WT mice were quickly immersed in the prepared solution (solution 1 mixed with an equal volume of solution 2) for 14 days in the dark at room temperature. The brains were then transferred to solution 3 and left for 48 h at 4 °C. After staining, the brains were embedded in optimal cutting temperature compound and then cut into 100 μm sagittal sections with a freezing microtome (Leica CM1950, Wetzlar, Germany). The sections were then mounted on slides and dried overnight in the dark. Images were acquired using a Nikon A1 HD25 microscope with NIS-Elements software by multiple Z-stack capturing. Next, 3D images were composed by extended depth of focus, and the dendritic spines were quantified.

Morphology quantification of dendrites

Imaris software (ver. 9.5, National Institutes of Health, MD, USA) was used to analyze the Golgi staining of dendrites in cerebellar Purkinje cells and hippocampal neurons. The acquired 3D neuron images were imported into Imaris software and processed into flat 2D maximum-intensity projection images. Neuron reconstruction was performed using the filament tracer tool. The largest and thinnest diameters of the neuron were manually determined to generate dendrite starting and seed points. Adjusted thresholds for these points were required to automatically generate filaments in the neurons of interest, and some undetected or misidentified branches were corrected manually with the creation wizard. Data on the total number of dendrite segments at different levels and the number of dendritic spines were exported for statistical analysis.

Transmission electron microscopy

Tissue processing was performed as described previously [19]. Briefly, the mice were deeply anesthetized with urethane (1.0 g/kg) through the abdomen and perfused with 0.1 mol/L PBS followed by 4% PFA/2.5% glutaraldehyde in 0.1 mol/L PBS (pH 7.2). The mouse brains were dissected and postfixed in 1% OsO_4. Ultrathin sections were stained with lead citrate for electron microscopy imaging (JEOL JEM-1400 Flash, Akishima-shi, Japan).

Agilent Seahorse XF cell mito stress assay

To assess mitochondrial bioenergetic function, an Agilent Seahorse XF cell mito stress assay kit (Agilent Technologies, CA, USA) was used according to the manufacturer's protocol. *TMEM141* knockdown SH-SY5Y and WT SH-SY5Y cells were plated in a Seahorse XFe24 cell culture microplate and allowed to attach for 6−8 h before the addition of 150 μL of supplemental media. The oxygen consumption rate (OCR) was recorded followed by oligomycin injection in port A (56 μL) at a final concentration of 1.5 μM, FCCP injection in port B (62 μL) at a final concentration of 1.0 μM, and rotenone/antimycin injection in port C (69 μL) at a final concentration of 0.5 μM. Data analysis was performed using Report Generators software for the cell mito stress assay.

Quantification of copy numbers and breakpoint analysis

DDHD2 deletion variation was confirmed by quantitative PCR (qPCR) using a QuantStudio3 real-time PCR system (Applied Biosystems, CA, USA). The primer pair for qPCR was as follows: forward, 5′-TCGCAGTGTTTCC TTGAACT-3′; reverse, 5′-CATCCACACCAGTAGAAT GCA-3′. The relative copy number (RCN) of the target sequence was calculated by the $2^{-\Delta\Delta Ct}$ method. The copy numbers of *DDHD2* in normal individuals were used as controls. An RCN of approximately 0.5-fold indicated heterozygous deletion, and an RCN of 0-fold indicated homozygous deletion. Gap-PCR was performed using a primer pair (forward, 5′-ATAGAGTGGGGTGCAGAAG AATG-3′; reverse, 5′-CTCCCCAGAGTAAACATCCC AC-3′) located outside of the *DDHD2* deletion region.

The cycling profile was as follows: 35 cycles of 30 s denaturation at 95 °C, 30 s annealing at 60 °C, and 3 min extension at 72 °C. Approximately 2 kb gap-PCR products were subjected to 2% agarose gel electrophoresis and subjected to Sanger sequencing after purification.

Statistical analysis

All the data were presented as mean ± SE and were analyzed using GraphPad Prism 6.0 software (GraphPad Software, CA, USA) or SPSS 19.0 software (SPSS, IL, USA). Comparisons between two groups were performed using Student's *t*-test or analysis of variance (ANOVA), followed by Tukey's post hoc test when the data exhibited a normal distribution in the Shapiro–Wilk normality test. The standard error (SE) of the mean normalized to the negative control was determined using the delta method [20]. Independent-sample *t*-test or single-sample *t*-test was used to compare the data after delta adjustment. Continuous measurements were analyzed using repeated ANOVA followed by Bonferroni post hoc tests. A P value of < 0.05 indicated significant difference.

Results

Clinical features and genetic analysis of a pedigree with ID, spastic paraplegia, and deafness

Here, we recruited a four-generation Pakistani NDD family (Fig. 1A). The proband was a 20-year-old female who presented with severe ID, developmental delay, feeding difficulties, language delay, epilepsy, facial

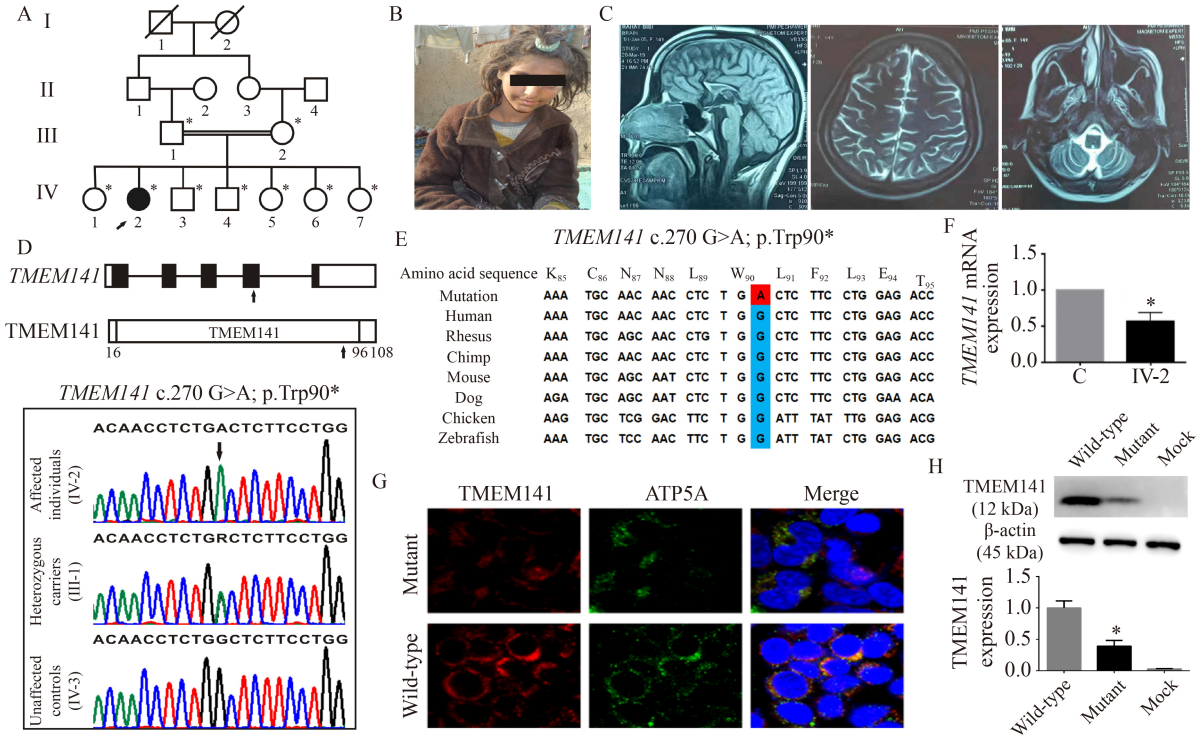

Fig. 1 Identification of a biallelic *TMEM141* variant in the individual from the family with neurodevelopmental disorders (NDDs). (A) Pedigree of a family with a *TMEM141* nonsense variant. The *TMEM141* variant cosegregated with the phenotype in this family as an autosomal recessive trait. The arrow indicates the proband, and the asterisks denote the individuals available for genotyping. (B) Facial photographs of IV-2 showing prominent eyes, mild hypertelorism (eyes were covered in consideration of the patient's privacy), a short nose with a flattened nasal bridge and a broad nasal base, mildly cupped ears, and a downturned upper lip. (C) Representative brain MRI of the proband (IV-2) showing diffuse subtle cerebral and cerebellar atrophy. (D) Schematic representation of the *TMEM141* gene and protein structure (top). Sanger sequence chromatograms of the proband and a heterozygous carrier of the *TMEM141* variant. Unaffected controls are also shown (bottom). The arrows indicate the sites of the *TMEM141* variant. (E) The Trp90 of TMEM141 is evolutionarily conserved among different species. (F) qRT–PCR of the relative *TMEM141* mRNA expression in peripheral blood lymphocytes from the proband and independent control. The data are presented as means ± SE ($n \geq 3$; $P < 0.05$). (G) IF staining for TMEM141 (red) and the mitochondrial marker protein ATP5A (green) indicated that the amounts of mutant protein were significantly reduced compared to those of the wild-type TMEM141 although the mutant protein was still located in the mitochondrion. (H) Immunoblotting of protein lysate from HEK293T cells transfected with wild-type or mutant plasmids showed that the mutant TMEM141 levels were reduced to approximately 40% of control levels. The gray intensity was analyzed using ImageJ software. The data are presented as means ± SE ($n \geq 3$; $P < 0.05$).

dysmorphism, and bilateral sensorineural hearing loss since childhood. Dysmorphic features included large eyes with mild hypertelorism, a short nose with a wide nasal bridge, slightly protruding ears, and a thin upper lip (Fig. 1B). She had hypertonia that was more prominent in the lower limb. Consistent with a recessive mode of inheritance, the proband was born to healthy first-cousin parents with an unremarkable pregnancy, delivery, and medical history. Brain MRI revealed diffuse subtle cerebral and cerebellar atrophy with prominent sulci and folia. Subtle fluid-attenuated inversion recovery along the bilateral medial temporal lobe and peritrigonal region was noted (Fig. 1C).

Many homozygosity blocks were identified in the proband's autosomes using genome-wide SNP genotyping, reflecting consanguinity in the family (Fig. S1A). To identify the causative variant, we performed WES analysis of the affected individual and her parents. We did not detect potential ID-causing single nucleotide variants that met our filtering criteria and only found one nonsense variant, c.270G>A (p.Trp90*) in *TMEM141* (referred to NM_032928.4), in the critical homozygous region on chromosome 9q34.3. The variant was confirmed by Sanger sequencing, and it cosegregated with the disease as a fully penetrant recessive trait in the family (Fig. 1D). This variant was predicted to be a disease- or damage-causing variant by prediction programs (MutationTaster, 1, disease causing; CADD–Phred, 37, damaging), and the Trp90 of TMEM141 was evolutionarily conserved across different species (Fig. 1E). It was absent in the public databases (gnomAD, dbSNP, and 1000 Genomes) and was not detected in chromosomes from 200 ethnically matched control individuals. The p.Trp 90* variant was predicted to result in degradation by the nonsense-mediated mRNA decay (NMD) of *TMEM141* or in the synthesis of truncated protein products lacking the last 18 amino acids. *TMEM141* showed medium-level damage in Gene Damage Index (GDI) Prediction (GDI–Phred, 0.909) at the mode of "Mendelian AR disease-causing genes". Therefore, the c.270G>A (p.Trp90*) variant in *TMEM141* may greatly affect phenotypes according to the prediction in CADD and GDI. Neither gnomAD nor the Database of Genomic Variants recorded homozygous LoF variants in *TMEM141* or copy number variations encompassing *TMEM141*. Overall, these findings suggested that AR TMEM141 deficiency is exceedingly rare in the general population and may be a disease-causing variant in the family.

Homozygous p.Trp90* variant in *TMEM141* causes deficiencies in *TMEM141* mRNA and protein expression

To evaluate the contribution of the p.Trp90* variant to *TMEM141* mRNA expression, we performed qRT–PCR in peripheral blood leucocytes. Approximately 40% reduction in the *TMEM141* mRNA level was detected in the affected individual (IV-2) compared with a control individual (C), indicating the partial degradation of the mutant transcripts (Fig. 1F). Subsequently, to further evaluate the contribution of the p. Trp90* variant to TMEM141 protein expression, we constructed WT and mutant *TMEM141* plasmids, expressed these constructs in HEK293T cells, and tested protein localization and expression. Immunofluorescence (IF) analysis revealed that although mutant protein was still located in the mitochondrion, the levels of mutant protein were significantly reduced compared with those of WT TMEM141 (Fig. 1G). Furthermore, immunoblot assays confirmed that the mutant TMEM141 levels were reduced to approximately 40% of the control levels in HEK293T cells overexpressing the WT or mutant protein construct, indicating that the p.Trp90* alteration destabilizes the TMEM141 protein (Fig. 1H). These results suggested that the nonsense variant in *TMEM141* exerts LoF effect through the NMD mechanism and decreased protein stability.

Expression profiles and intramitochondrial localization of the Tmem141 protein

We assessed the Tmem141 expression profiles in different mouse tissues. Tmem141 was initially expressed on the ninth day of embryonic development (E9) and reached a stabilized higher level seven days after birth (P7; Fig. 2Aa). Immunoblot assays showed that Tmem141 was highly expressed in the heart, kidney, brain, and liver and weakly expressed in the muscles, lungs, and spleen in WT mice at P60 (Fig. 2Ab). In the brain tissue, the cerebellum and hippocampus had the highest Tmem141 expression levels, followed by the cerebral cortex; however, low expression levels were observed in the basal ganglia and brainstem (Fig. 2Ac). We then tested the specific cellular location of *Tmem141* in the mouse brain using IF and IHC, revealing that *Tmem141* was highly expressed in the Purkinje cells of the cerebellum and hippocampal neurons (Figs. 2B and S2).

TMEM141 was reported as a mitochondrial transmembrane protein in the Human Protein Atlas database. To better explore the intramitochondrial localization of TMEM141, we constructed an APEX-TMEM141-fused plasmid, expressed it in HEK293T cells, performed DAB staining, and tested TMEM141 protein intramitochondrial localization using electron microscopy. As shown by electron microscopy, high-intensity signals were exclusively found in the outer mitochondrial membrane, suggesting that TMEM141 was a mitochondrial outer membrane protein (Fig. 2C).

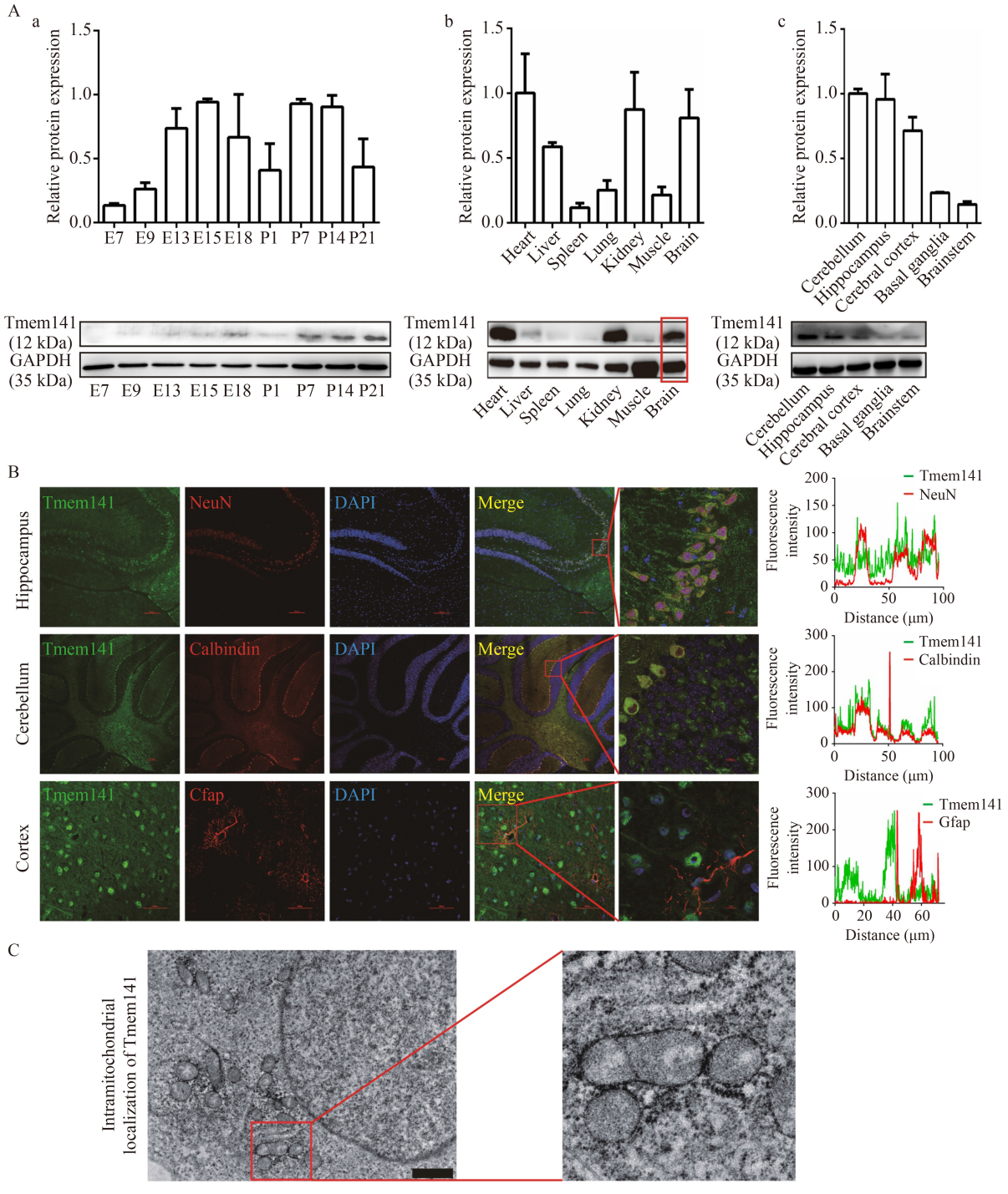

Fig. 2 Expression profiles and location of Tmem141 protein. (A) a. Tmem141 was initially expressed on the ninth day of embryonic development (E9) and reached a stabilized and high level 7 days after birth (P7); b. Immunoblot assays showing Tmem141 was highly expressed in the heart, kidney, brain, and liver and weakly expressed in the muscles, lungs, and spleen in the WT mice at P60; c. In the brain tissue, the cerebellum and hippocampus had the highest expression levels of Tmem141, followed by the cortex, but low expression levels were observed in basal ganglia and the brainstem. Gray intensity was analyzed using ImageJ software ($n \geqslant 3$). (B) IF staining for Tmem141 in the hippocampus, cerebellum, and cerebral cortex. Representative images showing colocalization of Tmem141 with the marker of hippocampal neurons, NeuN (up), and the marker of cerebellar Purkinje cells, calbindin (middle), but not the marker of astrocytes, Gfap (down). Scale bars: 100 μm. The fluorescence integrated density was measured using the Plot Profile tool of ImageJ software. (C) Electron microscopy of HEK293T cells transfected with the TMEM141-APEX plasmid indicated that TMEM141 was exclusively located in the outer mitochondrial membrane. Scale bar: 10 μm.

Establishment of the *Tmem141* KI mouse model and phenotype analysis

To obtain further support for the pathogenicity of the *Tmem141* variant *in vivo*, we generated a *Tmem141* KI mouse model by inducing the nonsense p.Trp90* variant in exon 4 of *Tmem141* by CRISPR–Cas9 technology (Fig. S3A and S3B, homozygous KI mice described as *Tmem141*$^{p.Trp90*/p.Trp90*}$, heterozygous as *Tmem141*$^{WT/p.Trp90*}$, and wild type as *Tmem141*$^{WT/WT}$). Western blot analysis showed that the expression of *Tmem141* was significantly reduced in the brains of *Tmem141*$^{p.Trp90*/p.Trp90*}$ mice (Fig. S3C and S3D). Interbreeding of the *Tmem141*$^{WT/p.Trp90*}$ mice yielded significantly reduced *Tmem141*$^{p.Trp90*/p.Trp90*}$ pups with an unexpected Mendelian ratio (Table S1), indicating that *Tmem141*-null mice exhibited partial embryonic lethality and *Tmem141* played a nonredundant role in the development of mice. Subsequently, the anatomical and histological abnormalities from the *Tmem141*$^{p.Trp90*/p.Trp90*}$ brain were assessed. No visible defects were observed in the sizes and structures of the dissected brains between *Tmem141*$^{p.Trp90*/p.Trp90*}$ and WT littermates at P60, consistent with our MRI results (Fig. S4A and S4B).

Given that the highest expression level of Tmem141 was observed in the heart, we evaluated the cardiac structure and function of *Tmem141*$^{p.Trp90*/p.Trp90*}$ mice by using M-mode ultrasonic testing. However, no obvious differences in echocardiographic parameters (RVFW, IVS, LVFW, EF, LVEDD, and LVESD) were found between the WT and KI littermates at P60 (Fig. S5), combined with the absence of cardiac phenotypes in our proband. We concluded that TMEM141 deficiency might not primarily affect the cardiac system.

Tmem141$^{p.Trp90*/p.Trp90*}$ mice exhibit impaired motor coordination and deficiencies in learning and memory

We focused on the function of *Tmem141* in the central nervous system and conducted a series of behavioral experiments to assess the motor and cognitive functions of *Tmem141*-deficient mice. The *Tmem141*$^{p.Trp90*/p.Trp90*}$ mice at P60 exhibited a significant reduction in time spent on the rotarod compared with WT littermates (Fig. 3A), suggesting that the LoF variant in *Tmem141* impaired balance and motor coordination. The *Tmem141*$^{p.Trp90*/p.Trp90*}$ mice at P60 displayed increased latency to reach the hidden platform during training sessions. The probe test showed that the *Tmem141*$^{p.Trp90*/p.Trp90*}$ mice spent less time in the target zone than the *Tmem141*$^{WT/WT}$ mice (Fig. 3C). Therefore, the *Tmem141*$^{p.Trp90*/p.Trp90*}$ mice showed deficiencies in hippocampus-dependent spatial learning and memory in the Morris water maze test. Passive avoidance memory requires proper functioning of the hippocampal formation. Thus, the step-down passive avoidance test was used to assess the degree of retention of a fear memory by measuring the latency time and error times for an animal to enter a place where it previously experienced mild electrical foot shocks during training sessions. The step-down passive avoidance test showed that the *Tmem141*$^{p.Trp90*/p.Trp90*}$ mice had a significantly decreased step-down latency, indicating that passive avoidance memory was impaired (Fig. 3B).

Tmem141$^{p.Trp90*/p.Trp90*}$ mice exhibit deficient synaptic plasticity in hippocampal neurons and abnormal dendritic branching in cerebellar Purkinje cells

Consistent with *Tmem141* tissue-specific expression pattern and previous behavioral studies, our behavior test results suggested that *Tmem141*$^{p.Trp90*/p.Trp90*}$ mutant mice displayed learning and memory impairments. Thus, we evaluated hippocampal long-term potentiation (LTP), a physiological form of synaptic plasticity involved in learning and memory. LTP was impaired in the *Tmem141*$^{p.Trp90*/p.Trp90*}$ mouse model, consistent with our behavioral experiment results (Fig. 4A).

To investigate whether motor incoordination and cognitive impairments were related to structural and functional synaptic defects, we explored alterations in these regions in the *Tmem141*$^{p.Trp90*/p.Trp90*}$ mice by investigating the morphology of hippocampal neurons and cerebellar Purkinje cells using Golgi staining given that Tmem141 was highly expressed in the hippocampus and cerebellum at the protein level, However, Golgi staining revealed that the hippocampal neurons of the *Tmem141*$^{p.Trp90*/p.Trp90*}$ mice showed typical filopodium and thin dendritic spines compared with those of the WT mice that often displayed stubby, mushroom, and branched types, suggesting that the synaptic plasticity of hippocampal neurons was affected (Fig. 4B and 4C). Additionally, different levels of dendritic branches of cerebellar Purkinje cells were calculated using Imaris software. *Tmem141*$^{p.Trp90*/p.Trp90*}$ mice showed fewer primary dendritic branches and fewer stretching directions of branches than *Tmem141*$^{WT/WT}$ mice (Fig. 4D–4F), indicating that the complexity of the dendritic branching pattern may decrease in *Tmem141*$^{p.Trp90*/p.Trp90*}$ mice. These events may affect the function of cerebellar Purkinje cells, further affecting the function of the cerebellum associated with motor coordination.

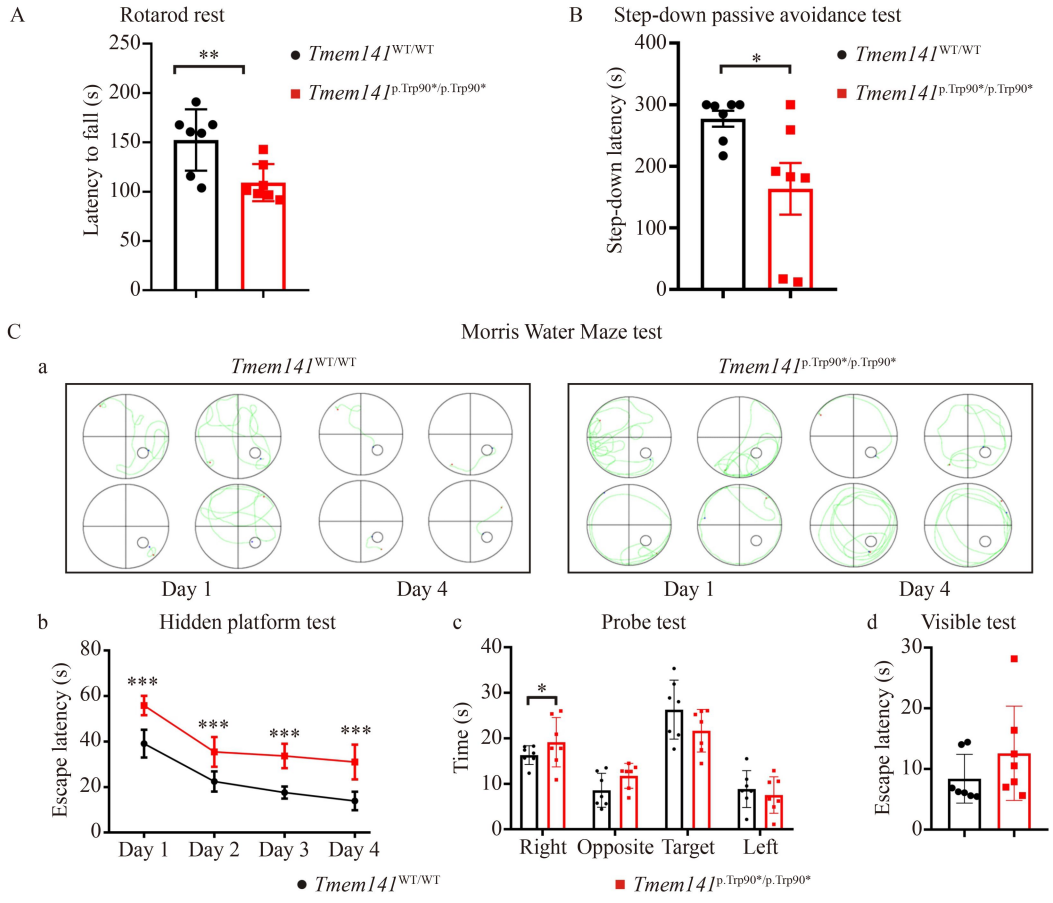

Fig. 3 Impaired motor coordination and learning ability of *Tmem141*$^{p.Trp90*/p.Trp90*}$ mice. (A) Rotarod test showing that the *Tmem141*$^{p.Trp90*/p.Trp90*}$ mice exhibited a significant reduction in time spent on the rotarod compared with WT littermates (n = 7; P < 0.01). (B) Step-down passive avoidance test displaying that the *Tmem141*$^{p.Trp90*/p.Trp90*}$ mice had a significantly decreased step-down latency compared with WT littermates (n = 7; P < 0.05). (C) Morris water maze test. a. Spatial search paths of *Tmem141*$^{p.Trp90*/p.Trp90*}$ and *Tmem141*$^{WT/WT}$ mice on the first day (day 1) and fourth day (day 4) in the hidden platform test. b. Hidden platform test showing that the *Tmem141*$^{p.Trp90*/p.Trp90*}$ mice exhibited increased latencies to reach the hidden platform compared with WT mice (n = 7; P < 0.001). c. Probe test showing that the *Tmem141*$^{p.Trp90*/p.Trp90*}$ mice spent less time in the target zone than WT mice (n = 7; P < 0.05). d. Visible test showing that compared with WT mice, *Tmem141*$^{p.Trp90*/p.Trp90*}$ mice exhibited slightly increased latencies to reach the visible platform (n = 7; P > 0.05). The mice used for behavioral experiments were all 2 months old.

TMEM141 deficiency may affect mitochondrial morphology and bioenergetic function

TMEM141 is a mitochondrial outer membrane protein; therefore, we examined mitochondrial morphology with electron microscopy. In contrast to regular WT mitochondria, mutant hippocampal neurons and cerebellar Purkinje cells aberrantly increased, enlarged mitochondria with irregular and swollen crests, and obvious cavitation, and their internal structures disappeared (Fig. 5A).

To assess mitochondrial function, we estimated ATP production rates and mitochondrial respiration with the Agilent Seahorse XF cell mito stress assay kit. *TMEM141* knockdown SH-SY5Y cell cultures were generated by stable infection with lentiviral vectors loaded with *TMEM141* shRNA, and cells infected with empty vectors were used as controls. SH-SY5Y cell cultures were seeded in a Seahorse XFe24 cell culture microplate, OCR was recorded, and oligomycin, FCCP, and rotenone/antimycin were injected. ATP production and mitochondrial respiration decreased when *TMEM141* was knocked down, suggesting that mitochondrial bioenergetic function was affected (Fig. 5B–5D).

Variants in *DDHD2* and *LHFPL5* cause spastic paraplegia and hearing loss

In addition to the nonsense variant in *TMEM141*, we found two variants in *DDHD2* and *LHFPL5* by WGS and WES analysis of the proband and her parents. These two variants were confirmed by Sanger sequencing. The variant in *DDHD2* cosegregated with spastic paraplegia, and the variant in *LHFPL5* cosegregated with hearing loss as a recessive trait in this family.

We found a homozygous intragenic deletion,

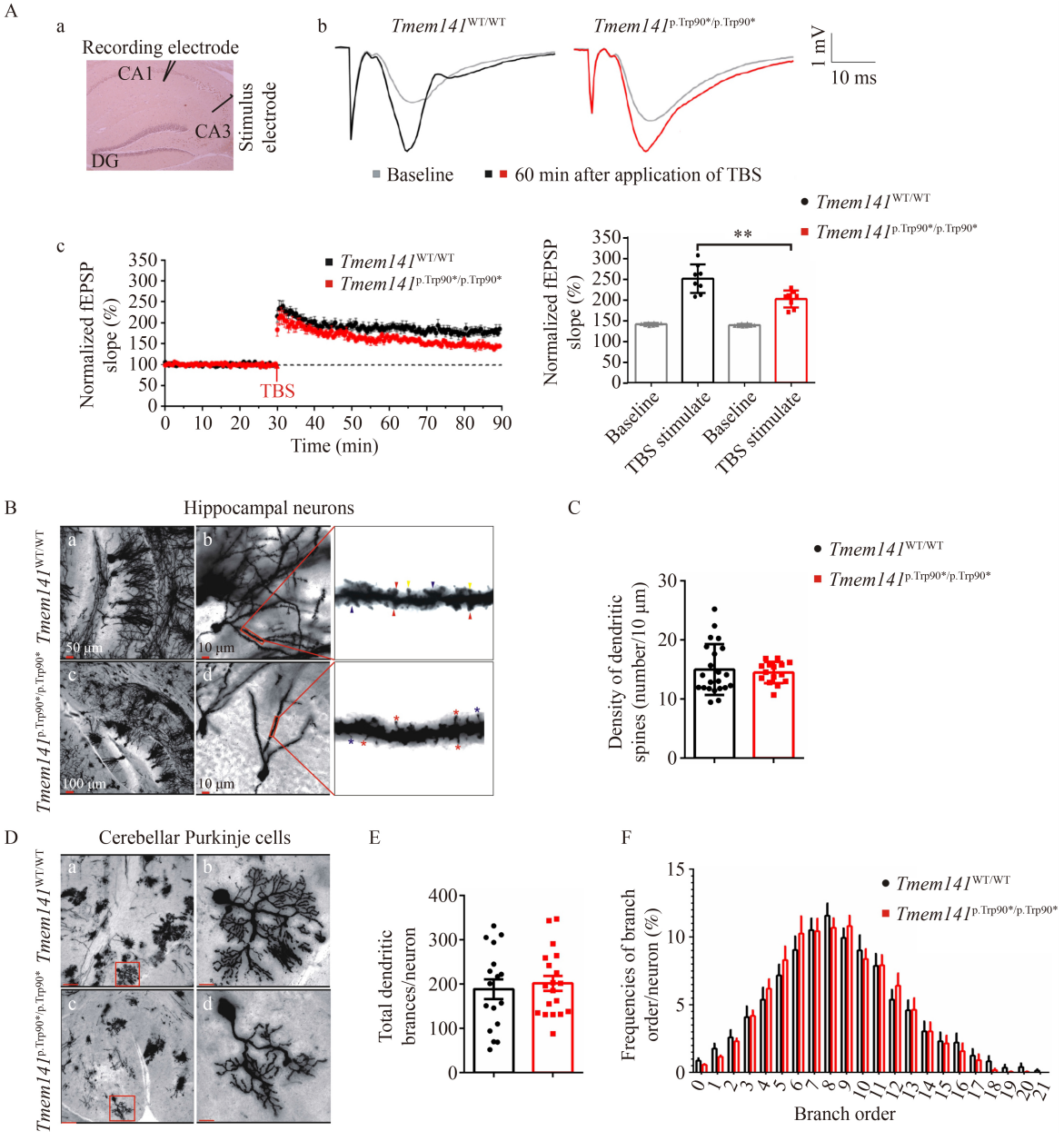

Fig. 4 Electrophysiological test and Golgi staining of hippocampal neurons and cerebellar Purkinje cells. (A) a. Position of stimulation and recording pipettes in hippocampal slices. b. fEPSPs recorded for each condition before (baseline) and 60 min after the application of theta-burst stimulation (TBS) in the hippocampal sections of the WT and *Tmem141*$^{p.\ Trp90*/p.\ Trp90*}$ mice. c. After TBS stimulation, the normalized fEPSP slope of the *Tmem141*$^{p.\ Trp90*/p.\ Trp90*}$ mice significantly decreased compared with that of the WT mice (n = 8; $P < 0.01$). (B) Golgi staining of mouse hippocampal neurons. Different types of dendritic spines are denoted (red arrowheads, stubby; yellow arrowheads, mushroom; blue arrowheads, branched; red asterisks, thin; and blue asterisks, filopodium). Scale bar in a: 50 μm; scale bar in c: 100 μm; scale bars in b and d: 10 μm. (C) Dendritic spine density of hippocampal neurons in *Tmem141*$^{p.\ Trp90*/p.\ Trp90*}$ and *Tmem141*$^{WT/WT}$ mice. A total of 18 neurons from three *Tmem141*$^{WT/WT}$ and 15 neurons from three *Tmem141*$^{p.\ Trp90*/p.\ Trp90*}$ mice were calculated. (D) Golgi staining of mouse cerebellar Purkinje cells. Scale bars in a and c: 100 μm; scale bars in b and d: 10 μm. (E) Total number of dendritic branches per neuron. (F) Frequencies of dendritic branches in different orders per neuron, indicating fewer primary branches and terminal branches in *Tmem141*$^{p.\ Trp90*/p.\ Trp90*}$ than in WT littermates. A total of 17 neurons from three *Tmem141*$^{WT/WT}$ mice and 19 neurons from three *Tmem141*$^{p.\ Trp90*/p.\ Trp90*}$ mice were calculated.

c.411+767_c.1249-327del, in *DDHD2* by WGS analysis of the proband (Fig. 6A), and it was validated by qPCR performed on a segment located in the deletion region (Fig. 6B). We amplified the deletion junction and confirmed a 14 028 bp deletion in this gene by Sanger sequencing (Fig. 6C and 6D). Deleterious variants in phospholipase *DDHD2* are associated with AR hereditary spastic paraplegia 54 (SPG54), which causes lower limb

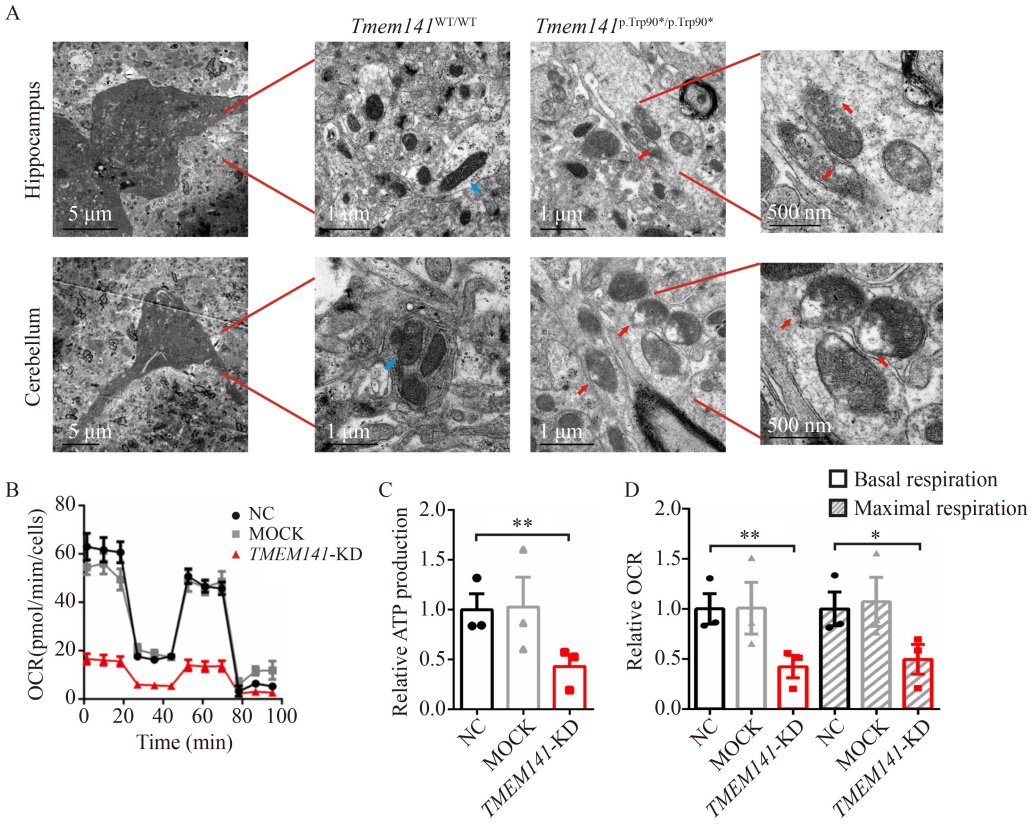

Fig. 5 Morphology and bioenergetic function of the mitochondrion were affected by *TMEM141* deficiency. (A) Electron microscopy of hippocampal neurons and cerebellar Purkinje cells aberrantly increased, enlarged mitochondria with irregular and swollen crests appeared, internal structures disappeared, and cavitation became prominent in the *Tmem141*$^{p.Trp90*/p.Trp90*}$ mice. (B) Normalized oxygen consumption rates (OCR) during a mitochondrial stress test for SH-SY5Y cell cultures (NC, wild-type SH-SY5Y cell cultures; MOCK, SH-SY5Y cells infected with empty vector; *TMEM141*-KD, SH-SY5Y cells infected with *TMEM141* shRNA vector). The results were normalized according to the number of cells in the NC group. (C) Relative ATP production of SH-SY5Y cell cultures in three different groups (normalized to the NC group). The results showed that reduced ATP was produced in *TMEM141*-KD cell cultures ($n = 5$; $P < 0.01$). (D) Basal respiration and maximal respiration of SH-SY5Y cell cultures in three different groups indicated weaker respiration in *TMEM141*-KD cell cultures than in the NC group ($n = 5$; $P < 0.05$).

spasticity, weakness, and ID [21]. The homozygous microdeletion we identified in *DDHD2* may account for motor impairments, hypertonia in the lower limb, and ID in the proband to a certain extent. In addition, we identified a homozygous one-nucleotide-deletion variant c.250delC (p.Leu84*) in the *LHFPL5* gene in the proband that was pathogenic for nonsyndromic hearing loss (NSHL) [22]. Therefore, severe bilateral sensorineural hearing loss presented in the proband may have resulted from this nonsense variant (Fig. S1B).

Discussion

NDD is a highly heterogeneous disease group with many biological pathways affected by pathogenic variants [23], reflecting the complexity of normal brain development [24]. Indeed, our NDD patient needed multiple molecular diagnostic approaches involving more than one clinical diagnosis and more than one genetic locus, each of which is segregated independently. Thus, panoramic variation analysis is imperative to analyze the disease phenotypes resulting from multilocus genomic variation [12].

In the present study, we characterized an NDD patient presenting with variable phenotypes of severe ID, spastic paraplegia, and deafness, who was born to consanguineous parents. Given that the heterogeneity of the clinical phenotype, panoramic variation analysis, pedigree analysis, SNP 6.0 array analysis, WES, WGS, and functional studies were applied to capture genotype–phenotype correlations or disease mechanisms. Pathogenic variants in *LHFPL5* cause AR NSHL [22]. The c.250delC (p.Leu84*) variant in *LHFPL5*, previously shown to be associated with NSHL [25], caused deafness in this family. In addition, disease-causing variants in *DDHD2* cause SPG54 [21], which belongs to a genetically heterogeneous group of disorders characterized by distal axonopathy of the corticospinal tract motor neurons. SPG54 mainly leads to early-onset spastic paraplegia, which may be accompanied by mild-to-moderate ID and movement impairments [26, 27]. A

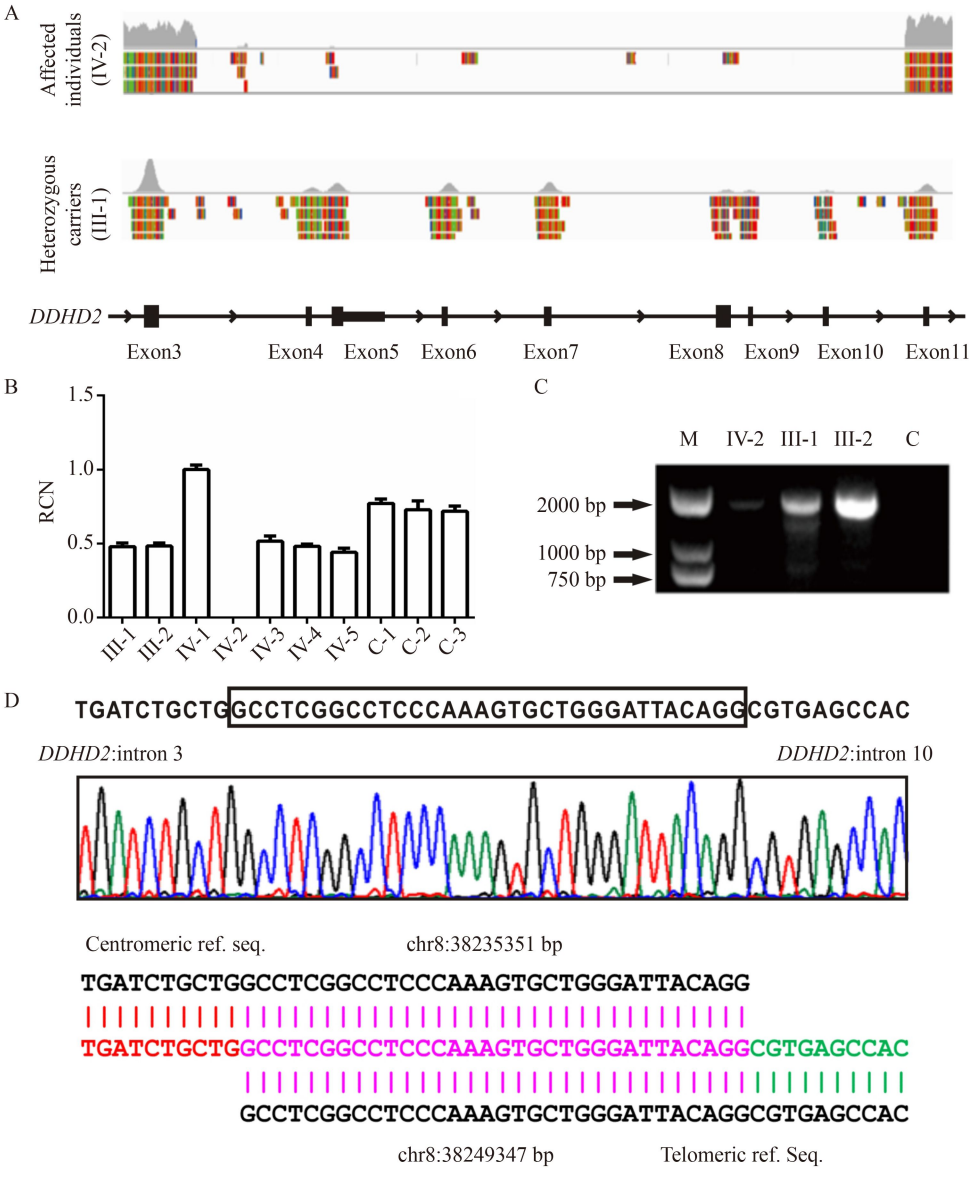

Fig. 6 Identification of the *DDHD2* deletion variant in the proband with NDDs. (A) IGV displaying the WGS results of IV-2 and WES results of III-1, indicating that the proband (IV-2) harbored a deletion variant from exon 4 to exon 10 of *DDHD2*. (B) qPCR of an amplicon located in the deletion region, validating the intragenic deletion. The values presented are the means of triplicate determinations ± SE. The unaffected individual (IV-1) was set to 1.0 relative copy number. (C) Amplification of the deletion junction showing cosegregation of the deletion variant with the phenotype in this family. M: marker. C: normal control. (D) Sanger sequence chromatograms and a schematic representation of the *DDHD2* deletion breakpoint. The overlapping sequence is highlighted.

novel intragenic deletion in *DDHD2* (c.411+767_c.1249-327del) was responsible for spastic paraplegia and ID to a certain extent in the affected family member. Given that the phenotype of severe ID was identified in our patient, we considered further variant detection to provide a more comprehensive explanation for her phenotype.

Notably, a novel homozygous nonsense variant was detected in *TMEM141* (c.270G>A, p.Trp90*) in the patient. *TMEM141* belongs to the transmembrane protein family, which is poorly characterized although essential for metastatic processes [28]. Additionally, some transmembrane protein family members have been associated with overlapping neurological manifestations. For example, variants in *TMEM65,* which encodes the mitochondrial inner membrane protein, result in mitochondrial myopathy with severe neurological manifestations [6], variants in *TMEM70* cause isolated ATP synthase deficiency and neonatal mitochondrial encephalocardiomyopathy [7], and variants in *TMEM147* cause ID with facial dysmorphism [8]. *TMEM63C*, which regulates the endoplasmic reticulum and mitochondrial morphology, is responsible for childhood-onset hereditary spastic paraplegia and ID [9]. Variants in *TMEM67* cause cerebellar atrophy, mild ID, adolescent-onset dementia,

vertical gaze palsy, and ataxia [10]. Furthermore, AR TMEM141 deficiency is exceedingly rare in the general population. Therefore, we speculated that LoF variants in *TMEM141* are disease-causing variants; however, the biological function of *TMEM141* must be extensively investigated. To explore its specific molecular function, we first located TMEM141 at the tissue level, revealing its ubiquitous expression in cerebellar Purkinje cells, hippocampal neurons, and cerebral cortical neurons in the brain. Our extensive behavioral analyses, including the Morris water maze, rotarod test, and step-down passive avoidance test, showed that the *Tmem141*$^{p.Trp90*/p.Trp90*}$ KI mice recapitulated a subset of behavioral symptoms found in patients with *TMEM141* variants, suggesting its role in motor coordination and learning ability. Additionally, TMEM141 was specifically expressed in the outer mitochondrial membrane. Mitochondria are fundamental components for metabolic homeostasis in all multicellular eukaryotes. Particularly in the nervous system, mitochondrion-generated ATP is required to establish appropriate electrochemical gradients and reliable synaptic transmission [29]. The dendritic, somatic, axonal, and presynaptic segments of neurons have different energy demands, which require local adaptation of energy supply and local cellular signals interconnecting neuronal and mitochondrial metabolic activity [30]. Outer-membrane proteins integrate mitochondria into the cellular environment, and dysfunction in mitochondrial outer membrane proteins leads to neurological impairment; for example, LoF variants in translocase of outer mitochondrial membrane 70 (*TOMM70,* MIM *606081) result in variable white matter disease and neurological phenotypes [31]. In our study, the disruption of this protein led to dysfunction in mitochondrial morphology and bioenergetic functions, including ATP production rates and mitochondrial respiration. Consequently, LTP and synaptic plasticity were impaired, leading to learning and memory defects, which may explain the neurodevelopmental characteristics of the patient. Whether TMEM141 is involved in the assembly of specific hippocampal circuits remains to be determined. In addition, TMEM141 is highly expressed in the heart; however, cardiac ultrasonography performed on the *Tmem141*$^{p.Trp90*/p.Trp90*}$ mice showed no obvious myocardial disease or significant impairment in morphology. This finding was consistent with the clinical phenotype in our patient. Generally, we identified a novel causative gene, *TMEM141,* responsible for ID and movement impairments. Because of our limited quantities of collected pedigrees and heterogeneity of the NDD clinical phenotype, we suggested that more cases of patients with *TMEM141* LoF variants must be reported to enhance our understanding of its comprehensive phenotype and explore its further biological functions.

In the present study, we concluded that high-throughput sequencing methods, such as WGS, can robustly strengthen the identification of disease–gene relationships. However, for clinically overlapping but distinct NDDs, panoramic variation analysis is suggested followed by analysis of multiple lines of independent evidence to trace multilocus genomic variation. In summary, panoramic variation analysis on a consanguineous couple segregating to one affected child with descent variants for NDD, spastic paraplegia, and deafness, revealed the multilocus genomic variants of *LHFPL5*, *DDHD2* and novel ID-causing gene *TMEM141*.

Acknowledgements

We would like to thank all the individuals for their collaboration. This work was financially supported by the National Natural Science Foundation of China (NSFC) (Nos. 82001221 and 81788101), the National Key Research and Development Program of China (Nos. 2022YFC2703900 and 2022YFC2703903), and the CAMS Innovation Fund for Medical Sciences (CIFMS) (Nos. 2021-I2M-1-018, 2022-I2M-JB-004 and 2017-I2M-B&R-05).

Compliance with ethics guidelines

Conflicts of interest Liwei Sun, Xueting Yang, Amjad Khan, Xue Yu, Han Zhang, Shirui Han, Xiaerbati Habulieti, Yang Sun, Rongrong Wang, and Xue Zhang declare that they have no conflict of interest.

The study was approved by Peking Union Medical College Institutional Review Board and the study was performed in accordance with the ethical standards as laid down in the 1964 *Declaration of Helsinki* and its later amendments or comparable ethical standards. Informed consent was obtained from the patient and her family members. All institutional and national guidelines for the care and use of laboratory animals were followed.

Electronic Supplementary Material Supplementary material is available in the online version of this article at https://doi.org/10.1007/s11684-023-1006-x and is accessible for authorized users.

References

1. Parenti I, Rabaneda LG, Schoen H, Novarino G. Neurodevelopmental disorders: from genetics to functional pathways. Trends Neurosci 2020; 43(8): 608–621
2. Vissers LE, Gilissen C, Veltman JA. Genetic studies in intellectual disability and related disorders. Nat Rev Genet 2016; 17(1): 9–18
3. Maulik PK, Mascarenhas MN, Mathers CD, Dua T, Saxena S. Prevalence of intellectual disability: a meta-analysis of population-based studies. Res Dev Disabil 2011; 32(2): 419–436
4. Mefford HC, Batshaw ML, Hoffman EP. Genomics, intellectual disability, and autism. N Engl J Med 2012; 366(8): 733–743
5. Hu H, Kahrizi K, Musante L, Fattahi Z, Herwig R, Hosseini M, Oppitz C, Abedini SS, Suckow V, Larti F, Beheshtian M,

Lipkowitz B, Akhtarkhavari T, Mehvari S, Otto S, Mohseni M, Arzhangi S, Jamali P, Mojahedi F, Taghdiri M, Papari E, Soltani Banavandi MJ, Akbari S, Tonekaboni SH, Dehghani H, Ebrahimpour MR, Bader I, Davarnia B, Cohen M, Khodaei H, Albrecht B, Azimi S, Zirn B, Bastami M, Wieczorek D, Bahrami G, Keleman K, Vahid LN, Tzschach A, Gärtner J, Gillessen-Kaesbach G, Varaghchi JR, Timmermann B, Pourfatemi F, Jankhah A, Chen W, Nikuei P, Kalscheuer VM, Oladnabi M, Wienker TF, Ropers HH, Najmabadi H. Genetics of intellectual disability in consanguineous families. Mol Psychiatry 2019; 24(7): 1027–1039

6. Nazli A, Safdar A, Saleem A, Akhtar M, Brady LI, Schwartzentruber J, Tarnopolsky MA. A mutation in the *TMEM65* gene results in mitochondrial myopathy with severe neurological manifestations. Eur J Hum Genet 2017; 25(6): 744–751
7. ČížkováA, Stránecký V, Mayr JA, Tesarová M, Havlícková V, Paul J, Ivánek R, Kuss AW, Hansíková H, Kaplanová V, Vrbacký M, Hartmannová H, Nosková L, Honzík T, Drahota Z, Magner M, Hejzlarová K, Sperl W, Zeman J, Houstek J, Kmoch S. TMEM70 mutations cause isolated ATP synthase deficiency and neonatal mitochondrial encephalocardiomyopathy. Nat Genet 2008; 40(11): 1288–1290
8. Thomas Q, Motta M, Gautier T, Zaki MS, Ciolfi A, Paccaud J, Girodon F, Boespflug-Tanguy O, Besnard T, Kerkhof J, McConkey H, Masson A, Denommé-Pichon AS, Cogné B, Trochu E, Vignard V, El It F, Rodan LH, Alkhateeb MA, Jamra RA, Duplomb L, Tisserant E, Duffourd Y, Bruel AL, Jackson A, Banka S, McEntagart M, Saggar A, Gleeson JG, Sievert D, Bae H, Lee BH, Kwon K, Seo GH, Lee H, Saeed A, Anjum N, Cheema H, Alawbathani S, Khan I, Pinto-Basto J, Teoh J, Wong J, Sahari UBM, Houlden H, Zhelcheska K, Pannetier M, Awad MA, Lesieur-Sebellin M, Barcia G, Amiel J, Delanne J, Philippe C, Faivre L, Odent S, Bertoli-Avella A, Thauvin C, Sadikovic B, Reversade B, Maroofian R, Govin J, Tartaglia M, Vitobello A. Bi-allelic loss-of-function variants in TMEM147 cause moderate to profound intellectual disability with facial dysmorphism and pseudo-Pelger-Huët anomaly. Am J Hum Genet 2022; 109(10): 1909–1922
9. Tábara LC, Al-Salmi F, Maroofian R, Al-Futaisi AM, Al-Murshedi F, Kennedy J, Day JO, Courtin T, Al-Khayat A, Galedari H, Mazaheri N, Protasoni M, Johnson M, Leslie JS, Salter CG, Rawlins LE, Fasham J, Al-Maawali A, Voutsina N, Charles P, Harrold L, Keren B, Kunji ERS, Vona B, Jelodar G, Sedaghat A, Shariati G, Houlden H, Crosby AH, Prudent J, Baple EL. TMEM63C mutations cause mitochondrial morphology defects and underlie hereditary spastic paraplegia. Brain 2022; 145(9): 3095–3107
10. Brancati F, Camerota L, Colao E, Vega-Warner V, Zhao X, Zhang R, Bottillo I, Castori M, Caglioti A, Sangiuolo F, Novelli G, Perrotti N, Otto EA; Undiagnosed Disease Network Italy. Biallelic variants in the ciliary gene TMEM67 cause RHYNS syndrome. Eur J Hum Genet 2018; 26(9): 1266–1271
11. Coon H, Darlington T, Pimentel R, Smith KR, Huff CD, Hu H, Jerominski L, Hansen J, Klein M, Callor WB, Byrd J, Bakian A, Crowell SE, McMahon WM, Rajamanickam V, Camp NJ, McGlade E, Yurgelun-Todd D, Grey T, Gray D. Genetic risk factors in two Utah pedigrees at high risk for suicide. Transl Psychiatry 2013; 3(11): e325
12. Posey JE, Harel T, Liu P, Rosenfeld JA, James RA, Coban Akdemir ZH, Walkiewicz M, Bi W, Xiao R, Ding Y, Xia F, Beaudet AL, Muzny DM, Gibbs RA, Boerwinkle E, Eng CM, Sutton VR, Shaw CA, Plon SE, Yang Y, Lupski JR. Resolution of disease phenotypes resulting from multilocus genomic variation. N Engl J Med 2017; 376(1): 21–31
13. Desmet FO, Hamroun D, Lalande M, Collod-Béroud G, Claustres M, Béroud C. Human Splicing Finder: an online bioinformatics tool to predict splicing signals. Nucleic Acids Res 2009; 37(9): e67
14. Martell JD, Deerinck TJ, Sancak Y, Poulos TL, Mootha VK, Sosinsky GE, Ellisman MH, Ting AY. Engineered ascorbate peroxidase as a genetically encoded reporter for electron microscopy. Nat Biotechnol 2012; 30(11): 1143–1148
15. Li D, Wei H, Zhang Z, Liang W, Stokke BG. Oriental reed warbler (*Acrocephalus orientalis*) nest defence behaviour towards brood parasites and nest predators. Behaviour 2015; 152(12–13): 1601–1621
16. Zhang Z, Hong J, Zhang S, Zhang T, Sha S, Yang R, Qian Y, Chen L. Postpartum estrogen withdrawal impairs hippocampal neurogenesis and causes depression- and anxiety-like behaviors in mice. Psychoneuroendocrinology 2016; 66: 138–149
17. Ballesta JJ, del Pozo C, Castelló-Banyuls J, Faura CC. Selective down-regulation of α4β2 neuronal nicotinic acetylcholine receptors in the brain of uremic rats with cognitive impairment. Exp Neurol 2012; 236(1): 28–33
18. Abrahamsson T, Lalanne T, Watt AJ, Sjöström PJ. Long-term potentiation by theta-burst stimulation using extracellular field potential recordings in acute hippocampal slices. Cold Spring Harb Protoc 2016; 2016(6): pdb.prot091298
19. He Q, Sha S, Sun L, Zhang J, Dong M. GLP-1 analogue improves hepatic lipid accumulation by inducing autophagy via AMPK/mTOR pathway. Biochem Biophys Res Commun 2016; 476(4): 196–203
20. Polli JE, Rekhi GS, Augsburger LL, Shah VP. Methods to compare dissolution profiles and a rationale for wide dissolution specifications for metoprolol tartrate tablets. J Pharm Sci 1997; 86(6): 690–700
21. Gonzalez M, Nampoothiri S, Kornblum C, Oteyza AC, Walter J, Konidari I, Hulme W, Speziani F, Schöls L, Züchner S, Schüle R. Mutations in phospholipase DDHD2 cause autosomal recessive hereditary spastic paraplegia (SPG54). Eur J Hum Genet 2013; 21(11): 1214–1218
22. Kalay E, Li Y, Uzumcu A, Uyguner O, Collin RW, Caylan R, Ulubil-Emiroglu M, Kersten FF, Hafiz G, van Wijk E, Kayserili H, Rohmann E, Wagenstaller J, Hoefsloot LH, Strom TM, Nürnberg G, Baserer N, den Hollander AI, Cremers FP, Cremers CW, Becker C, Brunner HG, Nürnberg P, Karaguzel A, Basaran S, Kubisch C, Kremer H, Wollnik B. Mutations in the lipoma HMGIC fusion partner-like 5 (LHFPL5) gene cause autosomal recessive nonsyndromic hearing loss. Hum Mutat 2006; 27(7): 633–639
23. Platzer K, Sticht H, Edwards SL, Allen W, Angione KM, Bonati MT, Brasington C, Cho MT, Demmer LA, Falik-Zaccai T, Gamble CN, Hellenbroich Y, Iascone M, Kok F, Mahida S, Mandel H, Marquardt T, McWalter K, Panis B, Pepler A, Pinz H, Ramos L, Shinde DN, Smith-Hicks C, Stegmann APA, Stöbe P, Stumpel CTRM, Wilson C, Lemke JR, Di Donato N, Miller KG, Jamra R. *De novo* variants in MAPK8IP3 cause intellectual disability with

variable brain anomalies. Am J Hum Genet 2019; 104(2): 203–212
24. Dulovic-Mahlow M, Trinh J, Kandaswamy KK, Braathen GJ, Di Donato N, Rahikkala E, Beblo S, Werber M, Krajka V, Busk ØL, Baumann H, Al-Sannaa NA, Hinrichs F, Affan R, Navot N, Al Balwi MA, Oprea G, Holla ØL, Weiss MER, Jamra RA, Kahlert AK, Kishore S, Tveten K, Vos M, Rolfs A, Lohmann K. *De novo* variants in TAOK1 cause neurodevelopmental disorders. Am J Hum Genet 2019; 105(1): 213–220
25. Wang R, Han S, Khan A, Zhang X. Molecular analysis of twelve Pakistani families with nonsyndromic or syndromic hearing loss. Genet Test Mol Biomarkers 2017; 21(5): 316–321
26. Schuurs-Hoeijmakers JH, Geraghty MT, Kamsteeg EJ, Ben-Salem S, de Bot ST, Nijhof B, van de Vondervoort II, van der Graaf M, Nobau AC, Otte-Höller I, Vermeer S, Smith AC, Humphreys P, Schwartzentruber J, Ali BR, Al-Yahyaee SA, Tariq S, Pramathan T, Bayoumi R, Kremer HP, van de Warrenburg BP, van den Akker WM, Gilissen C, Veltman JA, Janssen IM, Vulto-van Silfhout AT, van der Velde-Visser S, Lefeber DJ, Diekstra A, Erasmus CE, Willemsen MA, Vissers LE, Lammens M, van Bokhoven H, Brunner HG, Wevers RA, Schenck A, Al-Gazali L, de Vries BB, de Brouwer AP. Mutations in DDHD2, encoding an intracellular phospholipase A(1), cause a recessive form of complex hereditary spastic paraplegia. Am J Hum Genet 2012; 91(6): 1073–1081
27. Fink JK. Hereditary spastic paraplegia: clinico-pathologic features and emerging molecular mechanisms. Acta Neuropathol 2013; 126(3): 307–328
28. Marx S, Dal Maso T, Chen JW, Bury M, Wouters J, Michiels C, Le Calvé B. Transmembrane (TMEM) protein family members: Poorly characterized even if essential for the metastatic process. Semin Cancer Biol 2020; 60: 96–106
29. Norat P, Soldozy S, Sokolowski JD, Gorick CM, Kumar JS, Chae Y, Yağmurlu K, Prada F, Walker M, Levitt MR, Price RJ, Tvrdik P, Kalani MYS. Mitochondrial dysfunction in neurological disorders: exploring mitochondrial transplantation. NPJ Regen Med 2020; 5(1): 22
30. Kann O, Kovács R. Mitochondria and neuronal activity. Am J Physiol Cell Physiol 2007; 292(2): C641–C657
31. Dutta D, Briere LC, Kanca O, Marcogliese PC, Walker MA, High FA, Vanderver A, Krier J, Carmichael N, Callahan C, Taft RJ, Simons C, Helman G, Network UD, Wangler MF, Yamamoto S, Sweetser DA, Bellen HJ. *De novo* mutations in *TOMM70*, a receptor of the mitochondrial import translocase, cause neurological impairment. Hum Mol Genet 2020; 29(9): 1568–1579